GDCh Research Article Angewandte International Edition Chemie www.angewandte.org

How to cite: *Angew. Chem. Int. Ed.* **2025**, e202511262
doi.org/10.1002/anie.202511262

Photonic Pigments

Disordered Inverse Photonic Beads Assembled From Linear Block Copolymers

*Juyoung Lee, Hyeong Seok Oh, Soohyun Ban, Jinhyeok Cho, and Kang Hee Ku**

Abstract: Structurally colored colloids, or photonic pigments, offer a sustainable alternative to conventional dyes, yet existing systems are constrained by limited morphologies and complex synthesis. In particular, achieving angle-independent color typically relies on disordered inverse architectures formed from synthetically demanding bottlebrush block copolymers (BCPs), hindering scalability and functional diversity. Here, we report a conceptually distinct strategy to assemble three-dimensional inverse photonic glass microparticles using amphiphilic linear BCPs (poly(styrene-*block*-4-vinylpyridine), PS-*b*-P4VP) via an emulsion-templated process. By employing trans-1,2-dichloroethylene to promote interfacial water infiltration, nanoscale aqueous domains form within the organic phase and direct short-range-ordered pore structures. Evaporative solidification arrests these structures into porous photonic beads with angle-independent color. Systematic control of surfactant alkyl chain length and BCP molecular weight enables precise tuning of pore size, shell thickness, and visible-range optical output. Furthermore, post-chemical modification via quaternization of P4VP provides an orthogonal chemical handle to modulate interfacial instability and photonic behavior. This work expands the self-assembly capabilities of linear BCPs and establishes a modular, scalable platform for producing structurally and chemically programmable photonic pigments.

Introduction

Structural colors, responsible for the vivid hues of butterfly wings, peacock feathers, and beetle shells, arise from the interaction of light with nanoscale periodic architectures rather than from chemical pigments.[1,2] These colors are non-fading, environmentally benign, and resistant to photobleaching, making them attractive for sustainable alternatives in coatings, cosmetics, and display technologies. Inspired by such systems, synthetic photonic pigments, discrete micro- or nanoparticles that exhibit structural color, have emerged as a promising route toward scalable, long-lasting coloration.[3–6] Block copolymers (BCPs) offer molecular-level control over periodicity, enabling the design of photonic materials through self-assembly.[7,8] Most BCP-based systems form one-dimensional (1D) lamellar structures with alternating domains of differing refractive indices, which selectively reflect visible light.[9–12] These photonic crystals, commonly realized as thin films, offer tunable color but exhibit strong angle dependence and require precise control over molecular weight.[13]

To improve processability and expand geometries beyond planar configurations, recent advances have explored emulsion-templated self-assembly to produce photonic microparticles, often referred to as photonic pigments.[14,15] In these systems, solvent-evaporative emulsions serve as confined, dynamic templates that direct BCP organization into spherical microstructures with tailored internal order.[16–22] Most such particles adopt radial or axial lamellar morphologies, alternating high-refractive-index layers arranged concentrically or in parallel, that translate 1D photonic architectures into discrete, pigment-scale formats.[23,24] Optical functionality has been further enhanced by strategies such as homopolymer doping to tune domain spacing, swelling-deswelling dynamics for solvent responsiveness, and external field-driven orientation using gravitational or magnetic forces.[25–28] While these advances have improved color tunability and responsiveness, the underlying 1D periodicity constrains nanostructural diversity and inherently couples color to domain alignment and particle geometry.

As an alternative, inverse photonic glass architectures have emerged: three-dimensional porous microparticles with short-range-ordered structures that generate color through isotropic scattering from disordered yet correlated nanoscale pores.[29–31] In contrast to Bragg reflection from periodic lamellae, this scattering mechanism enables angle-independent coloration and reduces sensitivity to alignment or viewing direction. Rather than refining periodicity, this approach embraces structural disorder to unlock new optical regimes with enhanced design freedom. To date, bottlebrush

[*] J. Lee, H. S. Oh, S. Ban, J. Cho, Prof. K. H. Ku
School of Energy and Chemical Engineering, Ulsan National Institute of Science and Technology, Ulju-gun, UNIST-gil 50, Ulsan 44919, Republic of Korea
E-mail: kangheeku@unist.ac.kr

Additional supporting information can be found online in the Supporting Information section

block copolymers (BBCPs) have been predominantly used to realize inverse photonic glass structures, as their rigid backbones and densely grafted side chains facilitate the formation and stabilization of nanoscopic water domains within emulsion droplets.[32–34] Through tuning of side-chain rigidity, interfacial energy, and processing conditions, BBCP-based photonic pigments have been developed for applications ranging from eco-friendly coatings to optical security and sensing.[35–38] However, the synthesis of BBCPs involves multistep polymerizations and stringent control over architecture, limiting scalability. Their mechanical brittleness and low solubility further hinder processing and integration into functional systems. Moreover, the densely packed side chains restrict chemical modification, making it difficult to introduce reactive moieties, such as pyridine groups, that are essential for post-assembly functionalization and interfacial engineering.[39–41] These limitations motivate the exploration of alternative polymer architectures capable of forming inverse photonic glass structures while offering greater synthetic accessibility and functional versatility.

Linear block copolymers (LBCPs) offer a synthetically accessible and scalable alternative to bottlebrush systems, with broad tunability in molecular weight and block composition.[42] Despite these advantages, their application in three-dimensional photonic architectures has never been explored. The inherent chain flexibility and relatively low interfacial activity of LBCPs have historically hindered the formation of stable, porous networks within emulsion droplets.[43] For instance, amphiphilic BCPs incorporating a poly(ethylene oxide) (PEO) block frequently undergo excessive swelling, resulting in broad pore size distributions and poorly defined internal domains.[44] Such behavior complicates the control of organic solvent–surfactant interactions, which are crucial for achieving reproducible nanostructures. In emulsion-templated assembly, pore formation depends critically on interfacial instability, which arises from the competition between surfactant adsorption in the aqueous phase and BCP partitioning in the organic phase.[44–46] This balance dictates water domain formation, droplet morphology, and ultimately, the internal nanostructure. Achieving inverse photonic glass architectures from LBCPs, therefore, requires precise control over interfacial energy and solvent quality to promote sufficient water infiltration and phase separation.

Here, we demonstrate the formation of inverse photonic glass pigments by assembling amphiphilic LBCPs, specifically (PS-*b*-P4VP), within emulsion droplets stabilized by a mixed surfactant system composed of sodium alkyl sulfates and poly(vinyl alcohol) (PVA). The combined effects of surfactant alkyl chain length, PVA content, and the interfacial characteristics of trans-1,2-dichloroethylene (TDE) as the organic solvent create a finely balanced environment that promotes the formation of nanoscale aqueous domains within the dispersed phase.[47] These internal water domains act as dynamic templates for porosity, while TDE's low interfacial tension and high volatility facilitate water ingress and subsequent capillary-driven solidification. The structural evolution is further guided by the competitive adsorption of surfactant and copolymer at the oil-water interface, which governs interfacial instability and phase separation. By systematically tuning polymer molecular weight and surfactant chain length, we establish quantitative design rules to control pore size, shell thickness, and structural color across the visible spectrum. Furthermore, by leveraging the pyridine functionality of P4VP, we introduce post-modification by quaternization as a chemically orthogonal handle to tune interfacial behavior and expand the photonic tunability beyond that achievable through physical parameters alone. This dual control over structure and interfacial chemistry establishes LBCPs as a modular and scalable platform for the design of angle-independent, functionally tunable photonic pigments.

Results and Discussion

Figure 1a illustrates the fabrication process of photonic porous BCP microparticles using a flow-focusing microfluidic device. PS_{109k}-*b*-$P4VP_{27k}$, amphiphilic linear BCP with a cylinder-forming composition, was dissolved in TDE, a solvent selected for its low interfacial tension (~7–10 mN m^{-1}), high density, and volatility. These properties facilitate water infiltration into the organic phase during emulsification and support the formation of nanoscale aqueous domains that act as dynamic porogens. Control experiments with other solvents (e.g., toluene, dichloromethane) yielded irregular particles with weak or heterogeneous colors, underscoring that TDE's balanced interfacial tension, rapid evaporation, and density close to water are critical for stable pore nucleation and kinetic arrest of bicontinuous domains (Figure S1).To enable stable emulsification and promote interfacial instability required for pore templating, a mixed surfactant system comprising PVA and sodium sulfate anionic surfactants with different alkyl chain lengths (C_n, n = 9, 10, 12, 13, and 14) was employed. The surfactant blend balances viscosity and interfacial adsorption, allowing for precise droplet formation within the microfluidic channel (170 µm junction), producing monodisperse oil-*in*-water emulsions with an initial diameter of ~120 µm (Figure 1b). We note that microfluidics was employed in this study to yield highly monodisperse particles, as the structural color is strongly dependent on particle size. For large-scale production or when microfluidic fabrication is not feasible, conventional batch emulsification methods such as vortex mixing, homogenization, or SPG membrane emulsification can also be used to generate particles in bulk, albeit with broader size distributions.

As the internal solvent gradually evaporates, strong capillary forces induce droplet shrinkage and consolidation of the BCP network, resulting in solid particles with an average diameter of 48.2 µm (Figure 1c,d). Time-resolved optical microscopy (OM) of PS_{109k}-*b*-$P4VP_{27k}$ emulsions stabilized by sodium tetradecyl sulfate (C_n = 14) (Figure 1e) captures the morphological and optical evolution during this transition. Initially, co-adsorption of the BCPs and surfactants lowers the interfacial tension, leading to interfacial roughening and facilitating the penetration of water into the organic phase. At this stage, the emulsions appear optically transparent due to the low polymer concentration and the absence of organized nanostructures. As the solvent content decreases, the polymer

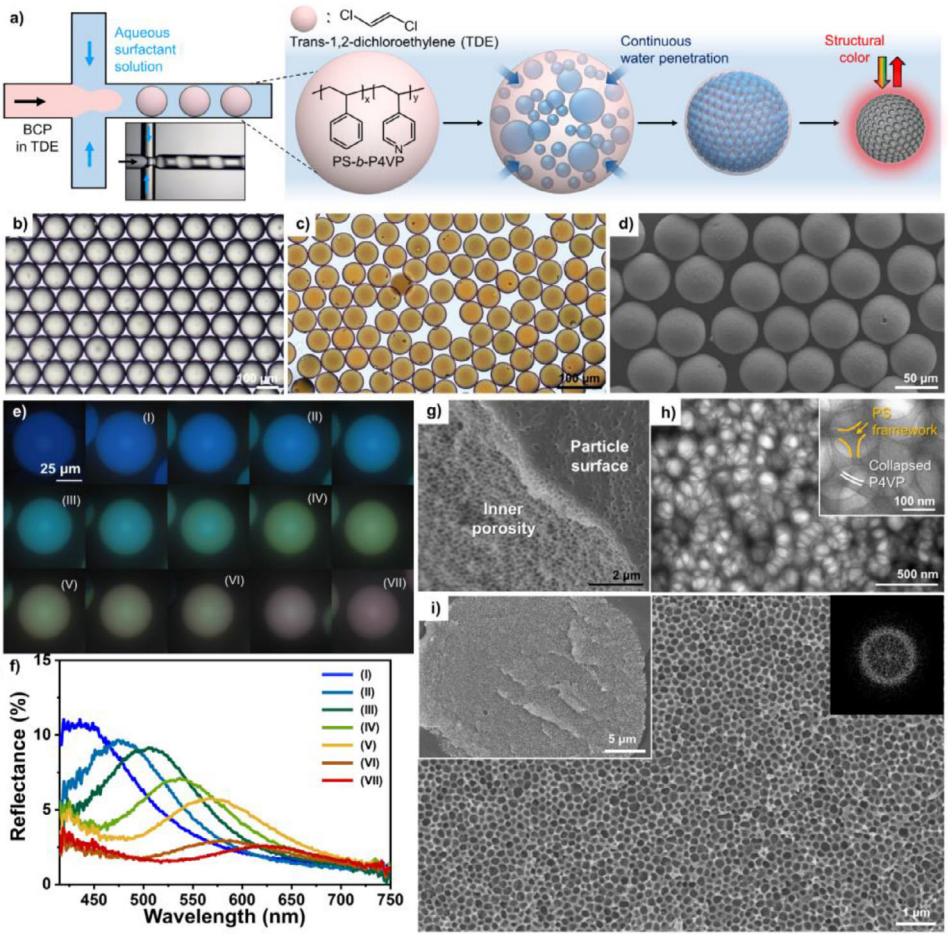

Figure 1. a) Schematic illustration of the fabrication process for porous microparticles from TDE-*in*-water emulsions using a flow-focusing microfluidic device; b) OM images of monodisperse PS_{109k}-*b*-$P4VP_{27k}$ emulsions before solvent evaporation; c) Transmittance OM image and d) low-magnification SEM image of porous PS_{109k}-*b*-$P4VP_{27k}$ particles; e) Time-dependent OM images of the PS_{109k}-*b*-$P4VP_{27k}$ emulsions in reflection mode during solvent evaporation and f) corresponding reflectance spectrum showing the evolution of structural color; g)–i) Cross-sectional SEM and TEM images of porous PS_{109k}-*b*-$P4VP_{27k}$ particles prepared by cryo-knife-sectioning and corresponding FFT analysis.

chains become progressively desolvated and begin to contract, increasing their packing density at the droplet interface.[45,48] This contraction drives phase separation between the PS and P4VP blocks, organizing internal water domains into a short-range-ordered porous network. Upon complete evaporation, the PS domains vitrify, fixing the porous architecture. Notably, the inward contraction of the polymer matrix exerts compressive stress on the aqueous domains, causing them to expand and stabilize into larger pores.[49] As a result, the average optical periodicity increases, leading to a redshift in structural color from ~420 to ~627 nm, as summarized in Figure 1f. Comparable structural evolution was observed in particles prepared using sodium dodecyl sulfate (C_n = 12), where sky blue coloration emerged upon drying (Figure S2). In both cases, the resulting particles exhibit uniform color across their surfaces, as indicated by broad and angle-independent reflection spots. This homogeneity arises from isotropic light scattering within a short-range-ordered, three-dimensional porous architecture, in contrast to lamellar systems where color is typically confined to central regions due to directional domain alignment.

To evaluate the internal morphology of the porous PS_{109k}-*b*-$P4VP_{27k}$ particles, we conducted scanning electron microscopy (SEM) and transmission electron microscopy (TEM) analyses. Knife-sectioned particles (Figure 1g,h) reveal a well-defined porous structure extending from the outer surface toward the core. The network consists of a continuous PS matrix that serves as the mechanical framework, with pores stabilized by the surrounding P4VP domains. (Figure 1i) further confirms the structural uniformity across the entire cross-section. The Fast Fourier transform (FFT) of the SEM image shows the representative short-range ordered pattern of pores within the inverse photonic glass particle. The pore diameter remains consistent throughout the particle (139 ± 17 nm), and the shell thickness exhibits minimal variation (33 ± 3 nm), indicating homogeneous solidification during solvent removal. These morphological characteristics align with the optical homogeneity observed in reflectance measurements and support that solvent-guided phase separation leads to short-range-ordered porous networks capable of producing isotropic structural colors through coherent scattering.

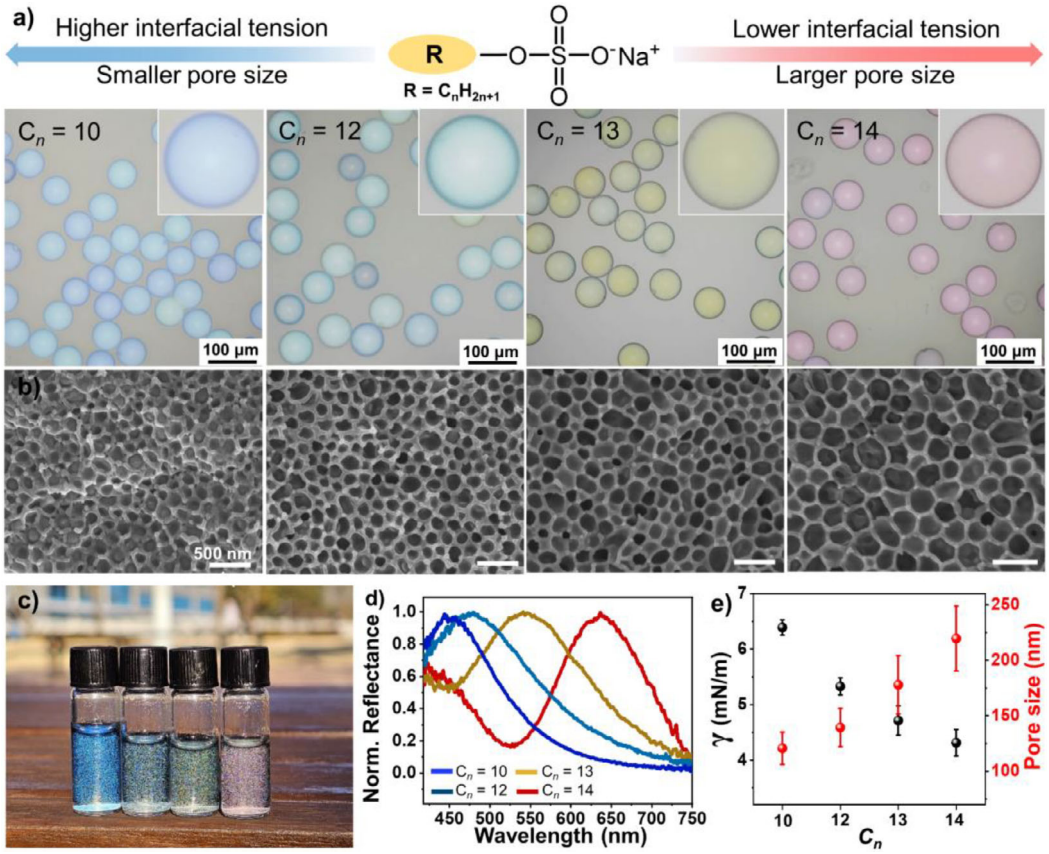

Figure 2. a) OM images in reflection mode and b) cross-sectional SEM images of PS_{109k}-*b*-$P4VP_{27k}$ photonic particles prepared using sodium sulfate anionic surfactant with varying alkyl chain lengths (C_n, n = 10, 12, 13, and 14); c) Bulk suspension image of each photonic particles under sunlight; d) Reflectance spectra of PS_{109k}-*b*-$P4VP_{27k}$ photonic particles corresponding to a); e) A plot of average pore diameters of PS_{109k}-*b*-$P4VP_{27k}$ particles and interfacial tension between polymer solution and aqueous surfactant solution as a function of C_n.

Surfactants play a crucial role in stabilizing oil-*in*-water emulsions by adsorbing at the oil-water interface, which directly influences droplet stability, interfacial tension, and polymer-water interactions. In particular, anionic sodium alkyl sulfate surfactants promote electrostatic interactions with the polar P4VP chains, enabling synergistic adsorption with PS-*b*-P4VP at the oil-water interface.[45] Control experiments showed that only anionic surfactants (SDS and sodium laurate) generated structurally colored porous particles, whereas nonionic PVA or cationic CTAB failed (Figure S3). SDS alone was effective but prone to sporadic aggregation, which was mitigated by co-adding PVA to enhance stability and reproducibility. Having established the specificity of anionic surfactants, we next investigated the effect of alkyl chain length on structural organization and optical properties by preparing PS_{109k}-*b*-$P4VP_{27k}$ particles with sodium sulfate surfactants of varying alkyl chain lengths (C_n, n = 10, 12, 13, and 14), while maintaining all other parameters constant (Figure 2). As the chain length increases, both the critical micelle concentration (CMC) and interfacial tension between the oil and water phases decrease, which enhances surfactant adsorption and promotes the formation of larger internal water domains. Reflective OM images (Figure 2a) show a clear red-shift in structural color with increasing alkyl chain length, transitioning from blue to cyan, green-yellow, and red colors for C_n = 10, 12, 13, and 14, respectively. Corresponding reflectance spectra (Figure 2d) confirm this trend, with representative peak wavelengths progressively shifting from 442 nm (C_n = 10) to 470, 571, and 637 nm (C_n = 14). According to Bragg's law ($\lambda = 2nd\sin\theta$), this redshift arises from an increase in average pore diameter (d), while the refractive index (n) and viewing angle (θ) remain effectively constant.[50] Cross-sectional SEM images and pore size distributions (Figures 2b and S4) further support this progressive increase in average pore diameter with increasing C_n: 120 ± 14 nm (C_n = 10), 139 ± 17 nm (C_n = 12), 177 ± 26 nm (C_n = 13), and 219 ± 29 nm (C_n = 14), while particle shell thickness remains relatively constant. These morphological changes directly translate into visible color variation in bulk suspension, as shown under natural lighting conditions (Figure 2c), demonstrating the visual tunability achieved through simple molecular-level adjustment of the surfactant. Consistently, macroscopic photographs under diffuse illumination confirm that the perceived color remains angle-independent, with no iridescence upon sample rotation (Figure S5).

The pore size increase can be attributed to enhanced surfactant adsorption and increased interfacial instability at the oil-water interface. To quantify this effect, interfacial tension values (γ) were measured with a pendant drop

Table 1: Summary of pore size, wall thickness, and maximum peak wavelength for porous photonic PS-*b*-P4VP particles, corresponding to the molecular weights used in this study.

Type of PS-*b*-P4VP	Pore Size (nm)	Wall thickness (nm)	λ_{max} (nm)
107k-*b*-18k	99.9 ± 10.29	34.9 ± 2.0	416 ± 8
106k-*b*-22k	115.5 ± 14.4	31.2 ± 3.6	437 ± 12
109k-*b*-27k	139.4 ± 17.2	33.6 ± 3.1	459 ± 15
120k-*b*-22k	189.7 ± 21.4	42.5 ± 3.6	593 ± 15
121k-*b*-35k	305.9 ± 28.5	46.2 ± 5.1	> 750

tensiometer, using aqueous surfactant solutions (10 mg mL^{-1}) and either pure TDE or TDE containing PS_{109k}-*b*-$P4VP_{27k}$ (10 mg mL^{-1}) (Figure 2e; Tables S1 and S2). In both cases, γ decreased with increasing alkyl chain length, reflecting chain-length-dependent lowering of interfacial free energy. The addition of PS-*b*-P4VP led to a steeper reduction in γ, indicating strong polymer-surfactant interactions that further destabilize the interface. In polymer-containing systems, γ dropped from 6.39 mN·m^{-1} (C_n = 10) to 5.33, 4.72, and 4.31 mN·m^{-1} for C_n = 12, 13, and 14, respectively, while values were slightly higher in the absence of polymer. Notably, comparison of PVA-only, SDS-only, and PVA/SDS-mixture systems (Table S2, each at 1 wt% and mixed in a 1:1 ratio) revealed clear co-adsorption at the interface, highlighting cooperative packing between the polymer and surfactants. Interfacial instability predominantly arises after solvent evaporation, when polymer concentration at the droplet interface sharply increases. Although direct dynamic measurements under such conditions remain experimentally challenging, similar interfacial destabilization phenomena have been reported by Zhu and co-workers,[51] supporting our interpretation. Taken together, these results demonstrate that the amphiphilic nature of PS-*b*-P4VP promotes cooperative interfacial adsorption, amplifies surfactant effects, and facilitates interfacial deformation during emulsification, thereby directing pore formation.

The structural color of porous BCP microparticles arises from nanoscale periodicity, which is governed by both the internal pore architecture and the refractive index contrast within the particle. While surfactant chemistry primarily dictates interfacial behavior and pore formation, the molecular weights of the PS and P4VP blocks provide an additional level of control over the photonic response. As shown in Figures 3a and S6, PS-*b*-P4VP particles prepared with different molecular weights: PS_{107k}-*b*-$P4VP_{18k}$, PS_{106k}-*b*-$P4VP_{22k}$, PS_{120k}-*b*-$P4VP_{22k}$, and PS_{121k}-*b*-$P4VP_{35k}$, exhibit distinct structural colors, reflecting variations in pore size and shell thickness. These parameters, summarized in Table 1, influence the effective optical path length, which in turn the reflection wavelength.

Despite a relatively narrow molecular weight range (125 to 156 kg mol^{-1}), systematic increases in P4VP molecular weight led to pronounced red-shifts in color. For example, within the PS_{107k} series, increasing the P4VP molecular weight from 18k to 22k (PS_{107k}-*b*-$P4VP_{18k}$ versus PS_{106k}-*b*-$P4VP_{22k}$) expands the average pore size from ~99 to ~115 nm and shifts the reflection color from violet to blue. A similar trend is observed in the PS_{120k} series, where increasing the P4VP block from 22k to 35k (PS_{120k}-*b*-$P4VP_{22k}$ versus PS_{121k}-*b*-$P4VP_{35k}$) enlarges the pore diameter from ~189 to ~305 nm and shifts the color from yellow-orange to the infrared region. This behavior can be rationalized by considering the effective packing parameter $P = v/a_0 l$, where v is the volume of the hydrophilic P4VP block, a_0 is the optimal interfacial area per chain, and l is the chain length. As the P4VP volume increases, the packing parameter rises, favoring the formation of emulsion droplets with reduced interfacial curvature and larger internal aqueous domains.[45,52] Upon solvent removal, these domains template the formation of larger pores, thus increasing the photonic periodicity and red-shifting the structural color. Additional insights arise from comparing PS_{106k}-*b*-$P4VP_{22k}$ and PS_{120k}-*b*-$P4VP_{22k}$, which share the same P4VP molecular weight but differ in PS length. PS_{120k}-*b*-$P4VP_{22k}$ forms a thicker shell (42 nm versus 31 nm), attributed to the increased hydrophobic block. Notably, despite sharing identical P4VP block length (22k), PS_{120k}-*b*-$P4VP_{22k}$ exhibits significantly larger pore size (189 nm) than PS_{106k}-*b*-$P4VP_{22k}$ (115 nm). This result, also observed in prior studies using PS-*b*-P4VP systems with constant f_{P4VP}, suggests that longer PS blocks expand the overall droplet and network dimensions, increasing the periodicity of interfacial undulation and enabling the formation of larger water domains during emulsification.[45] Such structural scaling, decoupled from packing parameter predictions, highlights the importance of total molecular size and interfacial roughness scale in defining final pore architecture.

In addition, blending two LBCPs with different molecular weights offers a tunable approach to modulate structural color across the visible spectrum. Figures 3c,d and S7 show the optical response of binary mixtures of PS_{109k}-*b*-$P4VP_{27k}$ (blue-reflecting) and PS_{121k}-*b*-$P4VP_{35k}$ (infrared-reflecting) at varying ratios. As the volume fraction of PS_{121k}-*b*-$P4VP_{35k}$ (f_{156k}) increases from 20 to 80%, the reflection peak redshifts from ~479 nm (sky blue) to ~653 nm (red), passing through green (~540 nm), and yellow (~557 nm), indicating a gradual increase in domain periodicity. As shown in cross-sectional images of Figure S8, the results clearly reveal a gradual increase in pore size as the fraction of the high-MW component increases, providing direct structural evidence for the gradient-like morphology and co-assembly of different MW chains. This continuous spectral shift is visualized in the CIE 1931 chromaticity diagram (Figure S9), where the color coordinates move from lower left (blue) to upper right (red) with increasing f_{156k}. The coordinates remain near the diagram center due to low color saturation, consistent with angle-independent, broadband reflection from short-range-ordered porous structures.[53] The spectral tunability arises from the co-assembly of the two LBCPs, where both species contribute to pore formation and domain modulation. Despite their molecular weight difference, the system forms a homogeneous porous network, as the shorter chains of PS_{109k}-*b*-$P4VP_{27k}$ enhance chain mobility and fill interstitial voids, promoting structural continuity.[54] Interfacial energy minimization further facilitates mixing, yielding a gradient-like domain distribution rather than distinct phase-separated regions. Similar behavior has been reported in binary bottle-

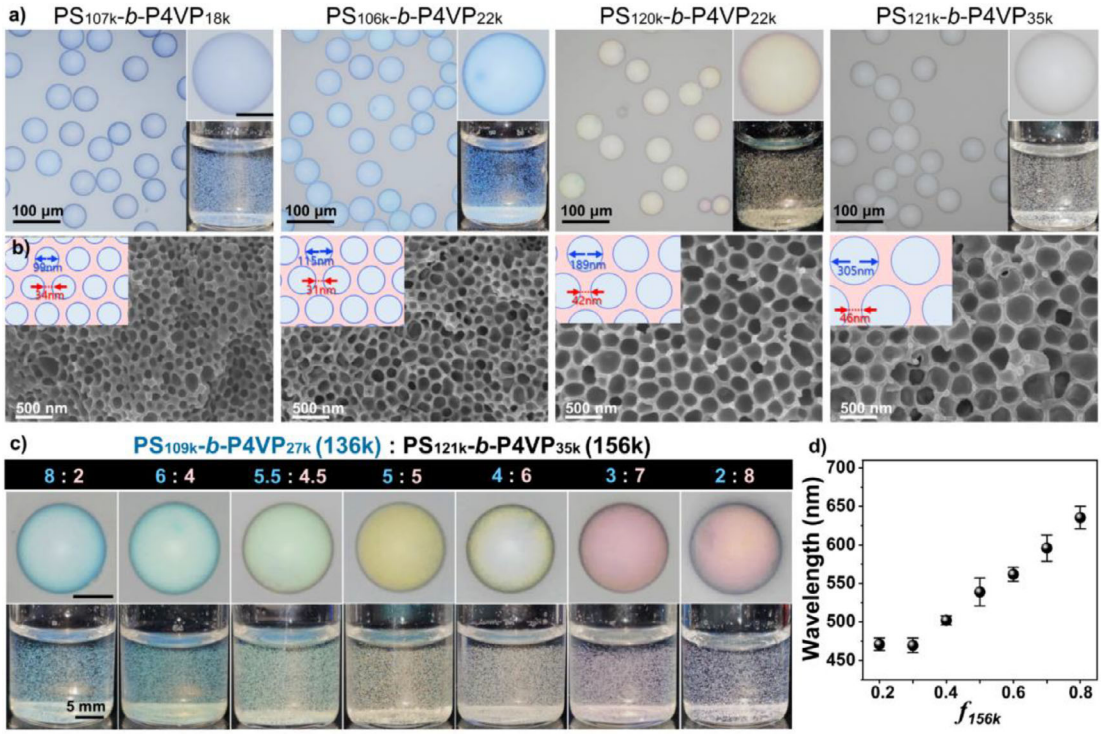

Figure 3. a) Photograph of bulk particle suspension, reflective OM images, along with b) cross-sectional SEM image of porous photonic PS-*b*-P4VP particles prepared using different molecular weights of PS_{107k}-*b*-$P4VP_{18k}$, PS_{106k}-*b*-$P4VP_{22k}$, PS_{120k}-*b*-$P4VP_{22k}$, and PS_{121k}-*b*-$P4VP_{35k}$. All particles were produced using surfactants with an alkyl chain length of $C_n = 12$; c) Reflective OM image and bulk particle suspension of a binary blend of PS_{109k}-*b*-$P4VP_{27k}$ and PS_{121k}-*b*-$P4VP_{35k}$ with varying volume ratios from 8:2 to 2:8; The scale bars are 20 μm. d) A plot of the peak wavelength of the particles as a function of the volume fraction of PS_{121k}-*b*-$P4VP_{35k}$ (f_{156k}) in the blend mixture.

brush copolymer systems when molecular weight disparity is small.[37] However, in contrast to BBCPs, the LBCP system achieves comparable spectral control within a narrower molecular weight window (125 to 156 kg mol^{-1}), highlighting its efficiency and scalability for structurally tunable, chemically versatile photonic pigment design.

Figure 4 summarizes the combined effects of both PS-*b*-P4VP molecular weight and the alkyl chain length of sodium sulfate surfactants on the nanoscale morphology and optical response of porous PS-*b*-P4VP particles. Three LBCPs: PS_{106k}-*b*-$P4VP_{22k}$, PS_{109k}-*b*-$P4VP_{27k}$, and PS_{120k}-*b*-$P4VP_{22k}$, were emulsified using sodium alkyl sulfate surfactants with C_n values ranging from 9 to 14 (Figures 4a and S10). The resulting structural colors span the ultraviolet to infrared range, illustrating how molecular architecture and interfacial chemistry jointly modulate photonic behavior.

Morphological analysis reveals that shell thickness is primarily determined by the PS block length and remains relatively constant across the surfactant series. PS_{106k}-, PS_{109k}-, and PS_{120k}-based particles exhibit average shell thicknesses of 31, 33, and 42 nm, respectively, with minimal variation as a function of C_n (Figures 4b, S11, and S12). In contrast, average pore diameter increases significantly with longer surfactant chains, and the magnitude of this increase is strongly dependent on polymer molecular weight. For PS_{106k}-*b*-$P4VP_{22k}$, increasing C_n from 9 to 14 enlarges the pore size from 75 ± 10 nm to 136 ± 16 nm. PS_{109k}-*b*-$P4VP_{27k}$ shows a broader range of increase (89 ± 8 nm to 219 ± 29 nm), while PS_{120k}-*b*-$P4VP_{22k}$ exhibits the most pronounced expansion, from 129 ± 18 nm to 268 ± 29 nm across C_n from 9 to 14. The extent of pore enlargement is markedly amplified in higher-molecular-weight LBCPs, suggesting that longer chains enhance the system's responsiveness to surfactant-mediated interfacial fluctuations. This behavior is attributed to the increased segmental mobility and interfacial coverage of longer chains during emulsification, which facilitates greater surfactant incorporation and more pronounced interfacial restructuring.[55] As a result, larger aqueous domains are stabilized within the droplets, which subsequently template expanded pore structures upon solidification.

The observed variations in pore size are directly reflected in the optical response, as shown in Figures 4c and S13. PS_{106k}-*b*-$P4VP_{22k}$ exhibits a modest shift from violet (~417 nm) to cyan (~476 nm), corresponding to a Δλ of ~50 nm when C_n varies from 10 to 13. PS_{109k}-*b*-$P4VP_{27k}$ displays a broader spectral shift from blue (~442 nm) to yellow (~571 nm) with a Δλ of ~120 nm. The most pronounced tunability is achieved with PS_{120k}-*b*-$P4VP_{22k}$, which transitions from green (~528 nm) to the infrared regime (~780 nm), yielding a total Δλ of ~250 nm and a colorless appearance under OM due to the reflection wavelength exceeding the visible range. These spectral changes are further captured in the CIE 1931 chromaticity diagram (Figure S14), where the coordinates shift progressively from blue to red with increasing surfactant chain length. At a given C_n, particles composed of higher-molecular-weight LBCPs exhibit larger displacements toward

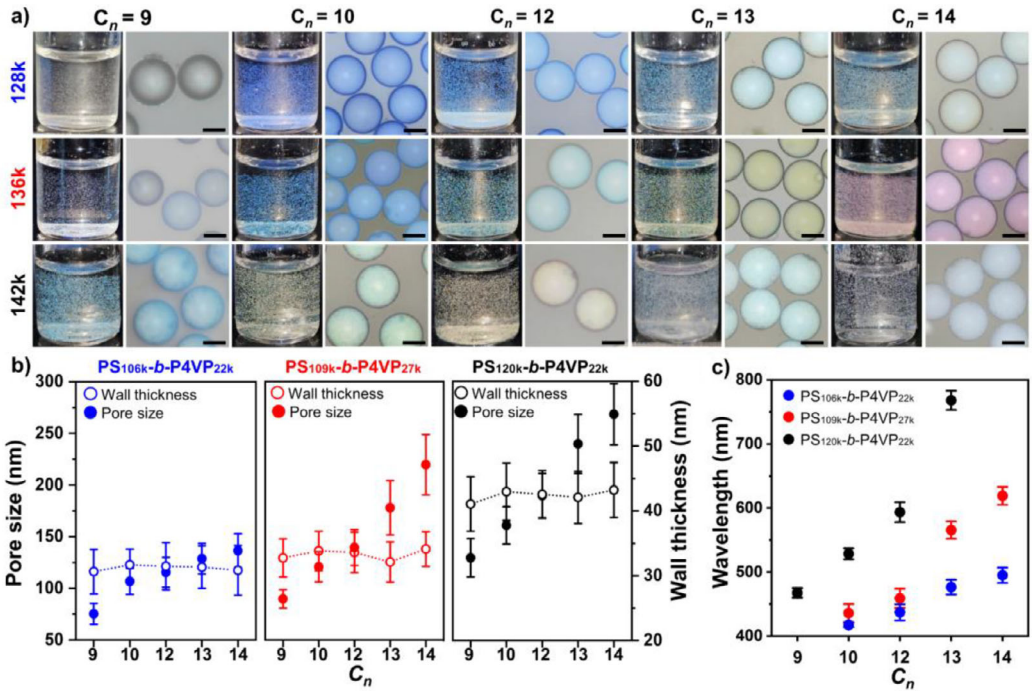

Figure 4. a) Bulk suspension photographs and reflective OM images of porous photonic PS-*b*-P4VP particles prepared with five different surfactant alkyl chain lengths (C_n, n = 9, 10, 12, 13, 14) for PS_{106k}-*b*-$P4VP_{22k}$, PS_{109k}-*b*-$P4VP_{27k}$, and PS_{120k}-*b*-$P4VP_{22k}$. The scale bars are 30 μm; b) Plots of average pore size (filled circle) and shell thickness (empty circle with dashed line) and as a function of C_n for each molecular weight; c) A plot of peak wavelength as a function of C_n for each molecular weight.

the upper-right region of the diagram, reflecting an increase in optical periodicity and red-shifted reflection. This trend emphasizes the cooperative role of BCP composition and interfacial chemistry in dictating structural color, suggesting the potential of LBCPs for designing full-spectrum, angle-independent photonic pigments with molecular-level tunability.

While structural coloration in LBCP-based inverse photonic glass particles can be finely tuned via molecular weight and surfactant chemistry, the presence of reactive pyridine units in P4VP offers an additional design rule unavailable in bottlebrush systems. Post-synthetic modification of these sites enables direct tuning of interfacial properties, such as electrostatic interactions, hydrophilicity, and steric environment, without altering the polymer backbone.[56,57] To leverage this chemical functionality, we systematically explored how the quaternization of P4VP with bromoalkane additives influences interfacial dynamics and structural coloration in LBCP-derived photonic pigments. By pre-mixing PS_{109k}-*b*-$P4VP_{27k}$ with varying molar ratios of bromoalkyl additives (i.e., 1-bromohexane (BrC_6), 1-bromooctane (BrC_8), and 1-bromodecane (BrC_{10})) prior to emulsification, we covalently functionalized pyridine moieties to yield quaternized PS-*b*-QP4VP (Figure 5a). The degree of quaternization, defined as f_{BrCn}, represents the molar ratio of bromoalkane to 4VP repeat units. FT-IR spectra (Figure S15) reveals the gradual emergence of pyridinium-associated bands, particularly the C=N stretching at 1625–1645 cm^{-1}, with increasing f_{BrCn}, consistent with progressive quaternization.[58] Complementary ^1H NMR analysis (Figure S16) further supports this, showing downfield shifts of pyridine protons and the appearance of alkyl-N^+-CH_2 resonances.[57] All emulsions were stabilized with SDS (C_n = 12) to ensure consistent interfacial conditions across the series.

Reflective OM images and corresponding bulk suspensions and reflection spectra (Figures 5b,c and S17) show that increasing f_{BrC6} induces a systematic redshift in structural color. At f_{BrC6} = 0.2, the particles exhibit a sky-blue reflection (~478 nm), similar to unmodified PS-*b*-P4VP, indicating minimal perturbation to the self-assembly. Increasing the quaternization to 0.4 and 0.6 shifts the peak to 534 nm (green) and 558 nm (green-yellow), respectively, followed by a pronounced red-shift to 641 nm at f_{BrC6} = 0.8. These shifts indicate that quaternization enhances the hydrophilicity of the P4VP domains, promotes interfacial destabilization, and facilitates water penetration, leading to pore expansion and red-shifted optical response. Notably, a comparison across the three bromoalkane additives highlights the critical role of alkyl chain length in modulating the photonic response. While BrC_6 enables full-spectrum modulation from blue to red, BrC_8 and BrC_{10} induce substantially smaller shifts at equivalent f_{BrCn}. For instance, particles prepared at f_{BrC8} = 0.8 reflect orange light (576 nm), while those with f_{BrC10} = 0.8 exhibit only a light green reflection (522 nm). At lower f, the latter two show minimal spectral change. This disparity arises primarily from the increasing hydrophobicity of longer alkyl chains, which offsets the hydrophilicity of the quaternized pyridinium groups and suppresses interfacial destabilization and water infiltration. In addition, the greater steric bulk of longer chains hinders access to pyridine moieties, reducing the overall quaternization efficiency and further limiting pore expansion.

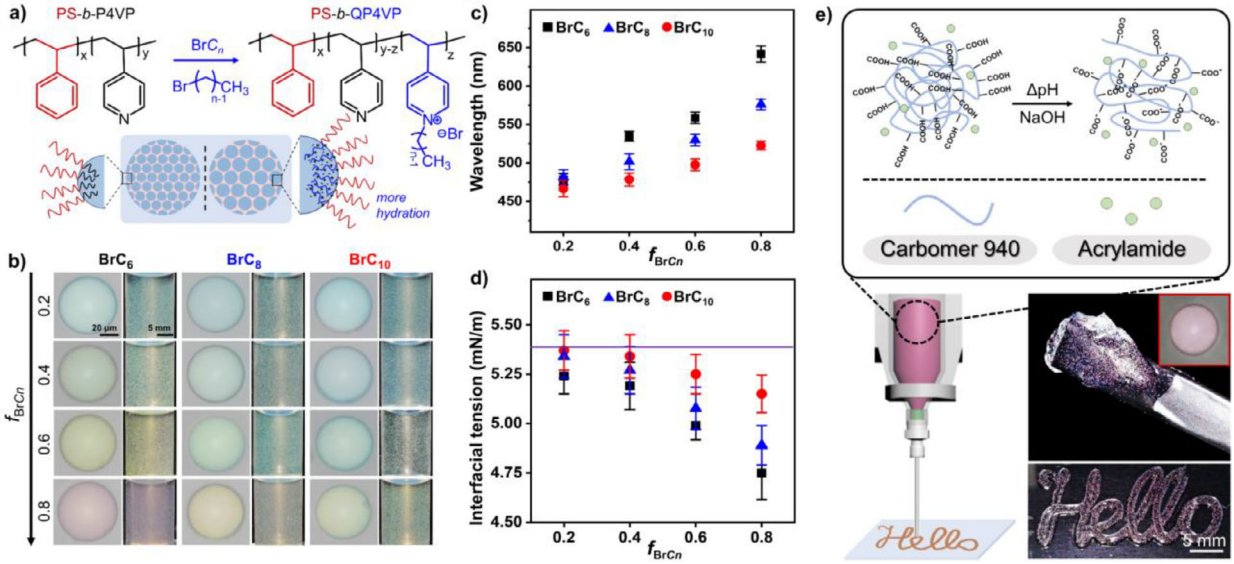

Figure 5. a) Schematic illustration for the co-assembly of PS-*b*-P4VP with bromoalkane additives (1-bromohexane (BrC_6), 1-bromooctane (BrC_8), and 1-bromodecane (BrC_{10})), highlighting the chemical tunability of the P4VP block via quaternization prior to assembly; b) Reflective OM images and corresponding bulk suspension photographs of PS_{109k}-*b*-$QP4VP_{27k}$ particles prepared with varying molar ratios of bromoalkane additives to P4VP units, denoted as $f_{BrCn} = 0.2$, 0.4, 0.6, and 0.8; c) Peak reflection wavelength and as a function of f_{BrCn} for each bromoalkene species; d) Interfacial tension between the quaternized PS-*b*-QP4VP solution and aqueous SDS solution as a function of f_{BrCn}. A purple line in the graph indicates the average interfacial tension of the pure polymer solution. e) Photographs of acrylamide-carbomer-based hydrogel ink with photonic microparticles; cursive "Hello" pattern printed on glass substrate.

To quantify this behavior, we measured the interfacial tension (γ) between the polymer solution and aqueous SDS as a function of f_{BrCn} (Figure 5d). For all additives, γ decreased with increasing quaternization, reflecting enhanced polymer amphiphilicity. However, the magnitude of reduction varied substantially with alkyl chain length: BrC_6 led to the greatest drop in average γ, from 5.2 to 4.7 $mN \cdot m^{-1}$, while BrC_{10} induced only a modest decrease over the same range, consistent with its limited optical tunability. Overall, these findings establish the quaternization of PS-*b*-P4VP as a modular and chemically orthogonal strategy for tuning interfacial behavior and structural color in LBCP-based photonic materials. Optical responsiveness depends not only on the degree of functionalization but also on the steric profile of the quaternizing agent. Short-chain bromides such as BrC_6 effectively promote interfacial reorganization and pore expansion, enabling full-spectrum color control through targeted post-chemical modification. This approach expands the design space for responsive photonic materials using synthetically accessible LBCPs.

Beyond structural and chemical tunability, we further evaluated the processability of the photonic particles by incorporating them into an acrylamide–carbomer hydrogel matrix (Figure 5e). The hydrogel effectively suppressed particle sedimentation, maintained optical transparency, and enabled homogeneous dispersion of the pigments. Notably, the hydrogel–particle composite could be readily extruded using a direct ink writing setup, forming patterned films that retained their angle-independent structural color. These results underscore that LBCP-derived photonic particles can be integrated into functional media and formulated into printable inks, thereby extending their applicability toward real-world optical and display technologies.

Conclusion

In this study, we developed a scalable strategy to fabricate inverse photonic glass microparticles from LBCPs, demonstrating that PS-*b*-P4VP can organize into three-dimensionally porous, photonic architectures without the need for bottlebrush backbones. As an evaporative solvent with low interfacial tension, trans-1,2-dichloroethylene allows for the stable development of a nanoscale aqueous domain and BCP porous structure. By systematically varying the molecular weight of BCPs and surfactant alkyl chain length, we established quantitative control over pore size, shell thickness, and structural color of the optical particle across the visible spectrum. Beyond physical design parameters in the BCP emulsion system, we introduced post-chemical modification via quaternization of the pyridine block to chemically modulate interfacial instability and broaden the optical tunability through electrostatic and steric design. This dual-level approach, combining structural design with reactive functionality, unlocks new opportunities for programmable coloration in soft materials. Nevertheless, the porous structures obtained from LBCPs show lower homogeneity and reflectance than those from bottlebrush BCPs, which benefit from intrinsic backbone rigidity. Yet, linear systems offer clear advantages in synthetic accessibility, modularity, and molecular design flexibility, making them attractive for scalable materials design. Looking ahead, enhancing effective rigidity (e.g., by alkyl modification of pyridine units) or moving

toward triblock architectures could provide finer control over interfacial curvature and pore ordering. Moreover, the pyridine block itself enables post-functionalization and ionic interactions, offering functional pathways not readily accessible with bottlebrush systems. Overall, our findings demonstrate LBCPs as a robust and modular platform for next-generation photonic pigments, offering synthetic simplicity, chemical adaptability, and broad applicability in coatings, sensors, and optical security materials.

Supporting Information

Additional characterization data (OM images and reflectance measurement of the photonic pigments, analysis of particle geometry). (PDF)

Acknowledgements

This research was supported by the National Research Foundation of Korea grant funded by the Korean government (RS-2024–00408989, RS-2024–00410962, and 2022R1C1C1006324) and Korea Toray Fellowship funded by Korea Toray Science Foundation.

Conflict of Interests

The authors declare no conflict of interest.

Data Availability Statement

The data that support the findings of this study are available in the Supporting Information of this article.

Keywords: Block copolymers · Inverse photonic glass · Photonic pigments · Self-assembly · Structure color

[1] S. Tadepalli, J. M. Slocik, M. K. Gupta, R. R. Naik, S. Singamaneni, *Chem. Rev.* **2017**, *117*, 12705–12763.
[2] Y. Zhao, Z. Xie, H. Gu, C. Zhu, Z. Gu, *Chem. Soc. Rev.* **2012**, *41*, 3297.
[3] C. Avci, M. L. De Marco, C. Byun, J. Perrin, M. Scheel, C. Boissière, M. Faustini, *Adv. Mater.* **2021**, *33*, 2104450.
[4] J. Ge, Y. Yin, *Angew. Chem. Int. Ed.* **2011**, *50*, 1492–1522.
[5] Z. Cai, Z. Li, S. Ravaine, M. He, Y. Song, Y. Yin, H. Zheng, J. Teng, A. Zhang, *Chem. Soc. Rev.* **2021**, *50*, 5898–5951.
[6] R. M. Parker, T. H. Zhao, B. Frka-Petesic, S. Vignolini, *Nat. Commun.* **2022**, *13*, 3378.
[7] H. S. Kang, S. W. Han, C. Park, S. W. Lee, H. Eoh, J. Baek, D.-G. Shin, T. H. Park, J. Huh, H. Lee, D.-E. Kim, D. Y. Ryu, E. L. Thomas, W.-G. Koh, C. Park, *Sci. Adv.* **2020**, *6*, eabb5769.
[8] S. Jeon, Y. L. Kamble, H. Kang, J. Shi, M. A. Wade, B. B. Patel, T. Pan, S. A. Rogers, C. E. Sing, D. Guironnet, Y. Diao, *Proc. Natl. Acad. Sci.* **2024**, *121*, e2313617121.
[9] Y. Kang, J. J. Walish, T. Gorishnyy, E. L. Thomas, *Nat. Mater.* **2007**, *6*, 957–960.
[10] H. Han, J. W. Oh, H. Lee, S. Lee, S. Mun, S. Jeon, D. Kim, J. Jang, W. Jiang, T. Kim, B. Jeong, J. Kim, D. Y. Ryu, C. Park, *Adv. Mater.* **2024**, *36*, 2310130.
[11] M. Stefik, S. Guldin, S. Vignolini, U. Wiesner, U. Steiner, *Chem. Soc. Rev.* **2015**, *44*, 5076–5091.
[12] T. H. Park, H. Eoh, Y. Jung, G.-W. Lee, C. E. Lee, H. S. Kang, J. Lee, K.-B. Kim, D. Y. Ryu, S. Yu, C. Park, *Adv. Funct. Mater.* **2021**, *31*, 2008548.
[13] J. K. D. Mapas, T. Thomay, A. N. Cartwright, J. Ilavsky, J. Rzayev, *Macromolecules* **2016**, *49*, 3733–3738.
[14] Y. Yang, H. Kim, J. Xu, M.-S. Hwang, D. Tian, K. Wang, L. Zhang, Y. Liao, H.-G. Park, G.-R. Yi, X. Xie, J. Zhu, *Adv. Mater.* **2018**, *30*, 1707344.
[15] S. Liu, Y. Yang, L. Zhang, J. Xu, J. Zhu, *J. Mater. Chem. C* **2020**, *8*, 16633–16647.
[16] X. Dai, X. Qiang, C. Hils, H. Schmalz, A. H. Gröschel, *ACS Nano* **2021**, *15*, 1111–1120.
[17] D. Klinger, C. X. Wang, L. A. Connal, D. J. Audus, S. G. Jang, S. Kraemer, K. L. Killops, G. H. Fredrickson, E. J. Kramer, C. J. Hawker, *Angew. Chem. Int. Ed.* **2014**, *53*, 7018–7022.
[18] S. G. Jang, D. J. Audus, D. Klinger, D. V. Krogstad, B. J. Kim, A. Cameron, S.-W. Kim, K. T. Delaney, S.-M. Hur, K. L. Killops, G. H. Fredrickson, E. J. Kramer, C. J. Hawker, *J. Am. Chem. Soc.* **2013**, *135*, 6649–6657.
[19] K. H. Ku, J. M. Shin, M. P. Kim, C.-H. Lee, M.-K. Seo, G.-R. Yi, S. G. Jang, B. J. Kim, *J. Am. Chem. Soc.* **2014**, *136*, 9982–9989.
[20] J. Kim, H. Yun, Y. J. Lee, J. Lee, S.-H. Kim, K. H. Ku, B. J. Kim, *J. Am. Chem. Soc.* **2021**, *143*, 13333–13341.
[21] J. J. Shin, E. J. Kim, K. H. Ku, Y. J. Lee, C. J. Hawker, B. J. Kim, *ACS Macro Lett.* **2020**, *9*, 306–317.
[22] R. Deng, J. Xu, G.-R. Yi, J. W. Kim, J. Zhu, *Adv. Funct. Mater.* **2021**, *31*, 2008169.
[23] Q. He, K. H. Ku, H. Vijayamohanan, B. J. Kim, T. M. Swager, *J. Am. Chem. Soc.* **2020**, *142*, 10424–10430.
[24] Y. Yang, Y. Chen, Z. Hou, F. Li, M. Xu, Y. Liu, D. Tian, L. Zhang, J. Xu, J. Zhu, *ACS Nano* **2020**, *14*, 16057–16064.
[25] Q. He, H. Vijayamohanan, J. Li, T. M. Swager, *J. Am. Chem. Soc.* **2022**, *144*, 5661–5667.
[26] Y. Yang, T.-H. Kang, K. Wang, M. Ren, S. Chen, B. Xiong, J. Xu, L. Zhang, G.-R. Yi, J. Zhu, *Small* **2020**, *16*, 2001315.
[27] K. Jo, J. Lee, J. Cho, K. H. Ku, *Macromolecules* **2025**, *58*, 3038–3047.
[28] J. Lee, S. Ban, K. Jo, H. S. Oh, J. Cho, K. H. Ku, *ACS Nano* **2024**, *18*, 5196–5205.
[29] C. I. Aguirre, E. Reguera, A. Stein, *Adv. Funct. Mater.* **2010**, *20*, 2565–2578.
[30] Y. Zhao, X. Zhao, J. Hu, M. Xu, W. Zhao, L. Sun, C. Zhu, H. Xu, Z. Gu, *Adv. Mater.* **2009**, *21*, 569–572.
[31] R. C. Schroden, M. Al-Daous, C. F. Blanford, A. Stein, *Chem. Mater.* **2002**, *14*, 3305–3315.
[32] A. L. Liberman-Martin, C. K. Chu, R. H. Grubbs, *Macromol. Rapid Commun.* **2017**, *38*, 1700058.
[33] H.-G. Seong, Z. Chen, T. Emrick, T. P. Russell, *Angew. Chem. Int. Ed.* **2022**, *61*, e202200530.
[34] H.-G. Seong, Z. Jin, Z. Chen, M. Hu, T. Emrick, T. P. Russell, *J. Am. Chem. Soc.* **2024**, *146*, 13000–13009.
[35] Q. Guo, R. Xue, J. Zhao, Y. Zhang, G. T. van de Kerkhof, K. Zhang, Y. Li, S. Vignolini, D.-P. Song, *Angew. Chem.* **2022**, *134*, e202206723.
[36] Z. Wang, R. Li, Y. Zhang, C. L. C. Chan, J. S. Haataja, K. Yu, R. M. Parker, S. Vignolini, *Adv. Mater.* **2023**, *35*, 2207923.
[37] X. Chen, D.-P. Song, Y. Li, *Macromolecules* **2022**, *55*, 7438–7445.
[38] B. Wang, K. Zhang, L. Pan, Y. Li, D.-P. Song, *Angew. Chem. Int. Ed.* **2025**, *64*, e202421315.
[39] J. Kim, J. Park, K. Jung, E. J. Kim, Z. Tan, M. Xu, Y. J. Lee, K. H. Ku, B. J. Kim, *ACS Nano* **2024**, *18*, 8180–8189.

[40] S. Yoo, J.-H. Kim, M. Shin, H. Park, J.-H. Kim, S.-Y. Lee, S. Park, *Sci. Adv.* **2015**, *1*, e1500101.
[41] D. Hu, Y. Wang, J. Liu, Y. Mao, X. Chang, Y. Zhu, *Nanoscale* **2022**, *14*, 6291–6298.
[42] H. Dau, G. R. Jones, E. Tsogtgerel, D. Nguyen, A. Keyes, Y.-S. Liu, H. Rauf, E. Ordonez, V. Puchelle, H. Basbug Alhan, C. Zhao, E. Harth, *Chem. Rev.* **2022**, *122*, 14471–14553.
[43] X. Chen, X. Yang, D.-P. Song, Y.-F. Men, Y. Li, *Macromolecules* **2021**, *54*, 3668–3677.
[44] J. Zhu, R. C. Hayward, *Angew. Chem. Int. Ed.* **2008**, *47*, 2113–2116.
[45] K. H. Ku, J. M. Shin, D. Klinger, S. G. Jang, R. C. Hayward, C. J. Hawker, B. J. Kim, *ACS Nano* **2016**, *10*, 5243–5251.
[46] X. Feng, X. Wang, D. Zhang, F. Feng, L. Yao, G. Ma, *Small* **2018**, *14*, 1703570.
[47] R. Deng, L. Zheng, X. Mao, B. Li, J. Zhu, *Small* **2021**, *17*, 2006132.
[48] Y. Wu, K. Wang, H. Tan, J. Xu, J. Zhu, *Langmuir* **2017**, *33*, 9889–9896.
[49] T. H. Zhao, G. Jacucci, X. Chen, D.-P. Song, S. Vignolini, R. M. Parker, *Adv. Mater.* **2020**, *32*, 2002681.
[50] Z. Wang, C. L. C. Chan, R. M. Parker, S. Vignolini, *Angew. Chem. Int. Ed.* **2022**, *61*, e202117275.
[51] J. Zhu, R. C. Hayward, *J. Colloid Interface. Sci.* **2012**, *365*, 275–279.
[52] A. H. Gröschel, A. Walther, *Angew. Chem. Int. Ed.* **2017**, *56*, 10992–10994.
[53] V. Hwang, A. B. Stephenson, S. Magkiriadou, J.-G. Park, V. N. Manoharan, *Phys. Rev. E.* **2020**, *101*, 012614.
[54] C. Choi, S. Ahn, J. K. Kim, *Macromolecules* **2020**, *53*, 4577–4580.
[55] R. Mészáros, I. Varga, T. Gilányi, *J. Phys. Chem. B* **2005**, *109*, 13538–13544.
[56] M. Ren, Z. Hou, X. Zheng, J. Xu, J. Zhu, *Macromolecules* **2021**, *54*, 5728–5736.
[57] Z. Tan, S. Ban, Y. Ahn, K. H. Ku, B. J. Kim, *Chem. Sci.* **2025**, *16*, 6265–6272.
[58] S. Ban, J. Lee, H. Kim, K. H. Ku, *ACS Appl. Mater. Interfaces* **2025**, *17*, 41154–41163.

Manuscript received: May 22, 2025
Revised manuscript received: August 19, 2025
Accepted manuscript online: August 29, 2025
Version of record online: ■■, ■■